Comparison of RF and High Impulse Magnetron Sputtered Gallium-Doped Zinc Oxide Thin Films

Justin Ryan Phelps *, Ashwin Kumar Saikumar 🆔, Reza Abdolvand and Kalpathy B. Sundaram

Department of Electrical and Computer Engineering (ECE), University of Central Florida, Orlando, FL 32816, USA
* Correspondence: justinp462@knights.ucf.edu

Abstract: For the first time in the literature, the material properties of gallium-doped zinc oxide, grown from a high impulse magnetron sputtering system (HiPIMS), are reported. These material properties are compared to those of a typical radio frequency (RF) sputtering deposition. The films were grown without thermal assistance and were compared across multiple average deposition powers. The films' resistivity, crystallinity, absorption coefficient, band gap, and refractive index were measured for each of the samples. It was observed that very similar results could be obtained between the HiPIMS and RF sputtering processes under the same average power conditions. It was found that the RF depositions demonstrated a slightly higher band gap and deposition rate as well as lower resistivity and optical absorption coefficient. Band gaps and grain size were found to increase with the power of the deposition for both HiPIMS and RF. These values ranged between 3.45 eV and 3.79 eV and 9 nm and 23 nm in this study, respectively. The absorption coefficient and resistivity were both found to decline with increasing power in both methods but reached minimums of 2800 cm^{-1} and 0.94 mOhm-cm, respectively, when sputtered using an RF power supply.

Keywords: gallium-doped zinc oxide; HiPIMS; RF; sputtering; conducting oxide

1. Introduction

Transparent conducting oxides (TCOs) allow for the conduction of electricity while maintaining a high level of optical transmissivity. This combination of properties is necessary for many modern devices such as displays, photovoltaics, light-emitting diodes, and sensors [1,2]. TCOs are created by doping metal oxides to create additional charge carriers while leaving the optical properties largely unchanged. There are two types of TCOs, N-type and P-type. N-type TCOs are generally preferred for electrode application due to their superior conductivity properties [3]. Zinc oxide is one of the most common ceramics used for creating N-type TCOs and has gained interest as a replacement for indium oxide due to the relative abundance of zinc and the rarity and toxicity of indium [4,5].

Much research has been conducted on the various deposition methods and dopants used in zinc oxide-based transparent conducting films. Both gallium and aluminum have been thoroughly investigated as dopants for zinc oxide. Gallium-doped zinc oxide (GZO) has shown several advantages over aluminum-doped zinc oxide (AZO). GZO has demonstrated superior environmental stability [6]. The figure of merit (FoM) for a TCO is defined by Haacke's equation ($\Phi = \frac{T^{10}}{R_{sh}}$), where T is the transmission of the thin layer at 550 nm and R_{sh} is the sheet resistance [7]. Considering this definition, using the proper deposition parameters GZO has been reported to have a higher FoM as compared to AZO [8]. Much research has been devoted to the deposition of GZO using various processing parameters and methods, such as RF and DC sputtering [9,10]. The results of these studies demonstrate that the method of deposition strongly influences the material properties of the thin films created. However, to our best knowledge, the material properties of high-impulse magnetron sputtering (HiPIMS) of GZO thin films have not been documented in the literature.

HiPIMS depositions often operate at similar average power levels to DC or RF deposition systems, however, the energy is applied over a shorter time interval increasing the peak instantaneous power of the deposition. This high-impulse power results in the ionization of the target material [11]. The HiPIMS process often results in thin film properties such as differing refractive index, film density, and hardness [12]. In another study, as compared to DC sputtering, HiPIMS-sputtered AZO thin films were shown to have lower resistivity [13]. For this reason, this study seeks to explore and report the material properties of GZO thin films created using HiPIMS for the potential benefits the unique material characteristics may offer electro-optical device designs as compared to other deposition methods.

In this paper, a comparative study of HiPIMS and RF deposition of GZO was conducted. In this study, the electrical, optical, and structural properties of the GZO thin films are compared across average deposition power values.

2. Materials and Methods

GZO films were deposited using an ultra-high vacuum AJA Orion 2 inch sputter system (AJA International, Inc., Scituate, MA, USA) with a Starfire Industries 2-2 pulsed power module (Starfire Industries, Champaign, IL, USA). Glass substrates were used to characterize the thin films. The substrates were cleaned using acetone, methanol, and isopropanol and subsequently dried in nitrogen. A 2 inch diameter zinc oxide/gallium oxide target 95/5 by weight percent with a purity of 99.998 percent from Kurt J Lesker (Kurt J. Lesker Company, Jefferson Hills, PA, USA) was used. A base pressure below 2.3×10^{-7} Torr was achieved before the deposition. The 13.56 MHz RF sputtering deposition power was swept from 50 W to 150 W, using ultra-pure grade Ar as the sputtering gas. This deposition was compared and contrasted with a HiPIMS deposition in which the average power was swept from 50 W to 150 W, as in the RF deposition. The HiPIMS experimental parameters can be found in Table 1.

Table 1. HiPIMS deposition parameters.

HiPIMS Sample	Frequency (Hz)	Pulse Width (μs)	Positive Kick Pulse Width (μs)	Peak Power (KW)	Average Power (W)
1	800	25	50	1.49	50
2	800	25	50	4.5	100
3	800	25	50	10.6	150

The Kick pulse width serves to increase the energy of the ionized target material and accelerate the ions toward the substrate [14]. These parameters were chosen for plasma stability and to be within typical HiPIMS parameters [15].

For both the RF and HiPIMS deposition, the pressure was maintained constant at 5 mTorr, and the Ar flow was kept constant at 20 sccm. All films were deposited over a 30 min interval which was preceded by 5 min of pre-sputtering with the target shield closed. To ensure film uniformity, the substrate was rotated at 20 RPM throughout the deposition. All films were deposited without thermal assistance.

The film thickness was characterized using a Veeco Dektak 150 profilometer (Veeco, Instruments Inc., Plainview, NY, USA). A PANalytical Empyrean XRD system (Malvern Panalytical, Westborough, MA, USA), using radiation from a Cu source at 45 kV and 40 mA, was used to obtain the XRD measurements with the diffraction patterns recorded between 2θ angles from 15–70 degrees. The grain size was determined using a field emission scanning electron microscope Zeiss ULTRA-55 FEG SEM (Zeiss Microscopy, White Plains, NY, USA). The surface roughness was determined using a Veeco 3100 AFM (Veeco, Instruments Inc., Plainview, NY, USA). A Cary 100 UV-Vis spectrophotometer (Varian Analytical Instruments, Walnut Creek, CA, USA) was used to measure the optical transmission over a wavelength range from 300−800 nm. The resistivity was determined by a Magne-Tron Instruments M-700 4-point probe (Magne-Tron Instruments, Palo Alto, CA,

USA) whose accuracy was confirmed with a known National Institute of Standards and Technology (NIST) calibration thin film. The conductivity type of the films was determined using the hot probe method.

3. Results

3.1. Deposition Rate

Each of the films in the experiment was deposited over a 30 min time interval. The film thicknesses were determined using lift-off and a profilometer to measure the thin film step. The average thicknesses of the films grown over the varying average powers can be seen in Figure 1 for each of the deposition methods.
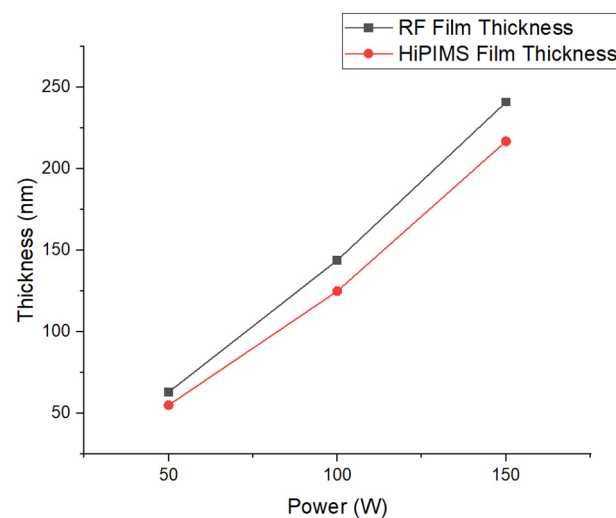
Figure 1. Plot of film thicknesses vs. average power for both RF and HiPIMS depositions.

Consistently, the RF sputtered thin film grew faster than the film grown by HiPIMS. This can be explained by the increased average kinetic energy in the sputtered HiPIMS material as compared to that of an RF deposition [16]. This increased energy of the bombarding ions may result in re-sputtering, which limits the growth rate of the film.

3.2. X-ray Diffraction

To observe the crystalline structure and grain size of the deposition, the deposited films were measured using X-ray diffraction analysis (XRD). The film's peak intensity increases as expected with thickness. Each film possessed a primary peak near 34 degrees which correspond to the (002) hexagonal zinc oxide wurtzite structure. A secondary peak is shown at approximately 62°, indicating the presence of (103) GZO structure growth as given by the JCPDS card of ZnO (JCPDS 36-1451). The lack of additional peaks indicates that all gallium within the film has been incorporated into the crystal or is interstitial within the structure, as the X-ray diffraction patterns lack peaks pertaining to gallium oxide's other phases or combinations of the present elements. The plot of the X-ray diffraction patterns can be seen in Figure 2.

The data from the XRD diffractogram results were used to calculate the grain size using the Debye–Scherrer equation [17]:

$$D = \frac{0.9\lambda}{B\cos\theta} \tag{1}$$

where B, θ, and λ are the full-width half maxima (FWHM), Bragg diffraction angle, and X-ray wavelength, respectively.
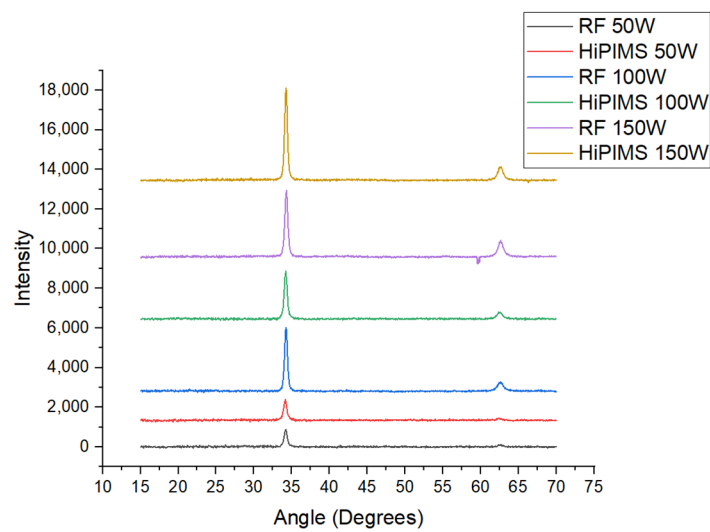
Figure 2. XRD diffractogram results displaying both the RF and HiPIMS depositions.

From the same data, the film stress was determined by relating the stress to the c lattice parameter. The c lattice constant is calculated as in [18]:

$$c = \frac{\lambda}{\sin \theta} \tag{2}$$

Using the strain-free lattice constant c_0 = 5.205 Å, the biaxial stress for the films may be calculated by [19]:

$$\sigma = \frac{-453.6 \times 10^9 (c - c_0)}{c_0} \tag{3}$$

The results of these calculations may be seen among the results reported in Table 2.

Table 2. Table of XRD, SEM, and AFM summary of data.

Sample	FWHM (rad)	Bragg Angle (rad)	c-Lattice Constant ($\times 10^{-10}$)	Scherrer Equation Grain Size (nm)	SEM Measured Grain Size	Calculated Film Stress (GPa)	Average Roughness (nm)
HiPIMS 50 W	0.0156	0.2982	5.242	9	10	−32.9	1.13
HiPIMS 100 W	0.0102	0.2978	5.250	14	15	−39.4	2.91
HiPIMS 150 W	0.0101	0.2989	5.232	14	22	−23.2	2.16
RF 50 W	0.0164	0.2987	5.235	9	10	−26.5	1.38
RF 100 W	0.009	0.2987	5.235	16	18	−26.5	1.62
RF 150 W	0.0095	0.2995	5.221	15	23	−13.6	2.20

3.3. Surface Morphology

The films' surface grains were examined using a scanning electron microscope. These images were then analyzed using image analysis software where the grain diameter of the film was determined as an average of the surface grain diameter. The results showed a clear correlation between the average power of the deposition and the surface grain size.

As expected, the surface grain size increased with increasing average power. The surface SEM images and reported grain measurements can be seen below in Figure 3 and Table 2, respectively.

HiPIMS Deposition   **RF Deposition**
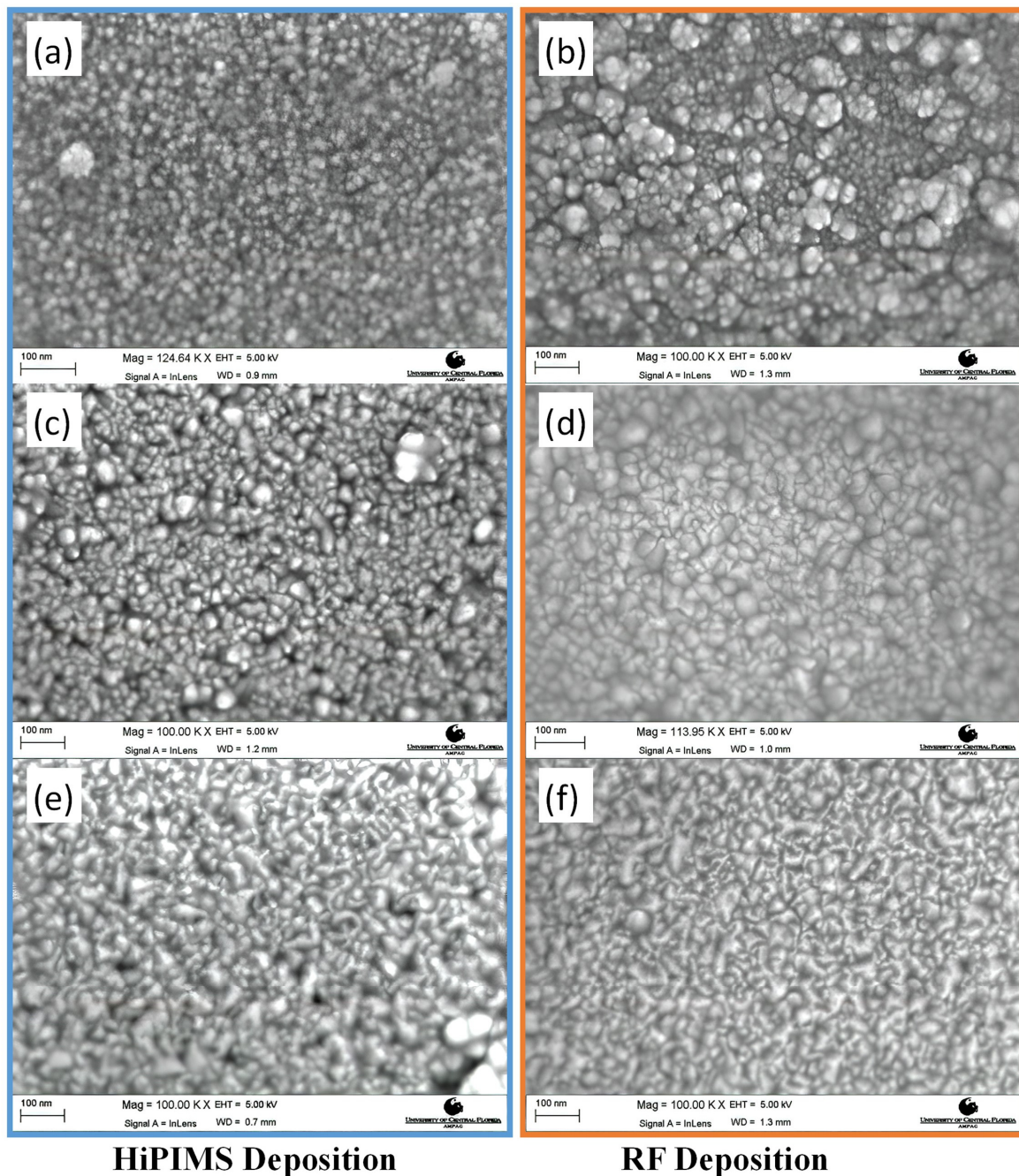
Figure 3. SEM images of the investigated depositions. (**a**): 50 W HiPIMS, (**b**) 50 W RF, (**c**) 100 W HiPIMS, (**d**) 100 W RF, (**e**) 150 W HiPIMS, (**f**) 150 W RF.

The larger surface grain size of the GZO thin film may be attributed to the increased surface energy of the incoming sputtered material.

The surface was further examined using atomic force microscopy. The grain size was measured again using the AFM measurements, and it was found to corroborate the results obtained from the SEM images. The surface morphology, as measured from the AFM, can be seen in Figure 4, along with the average surface roughness values for each deposition *Ra*.
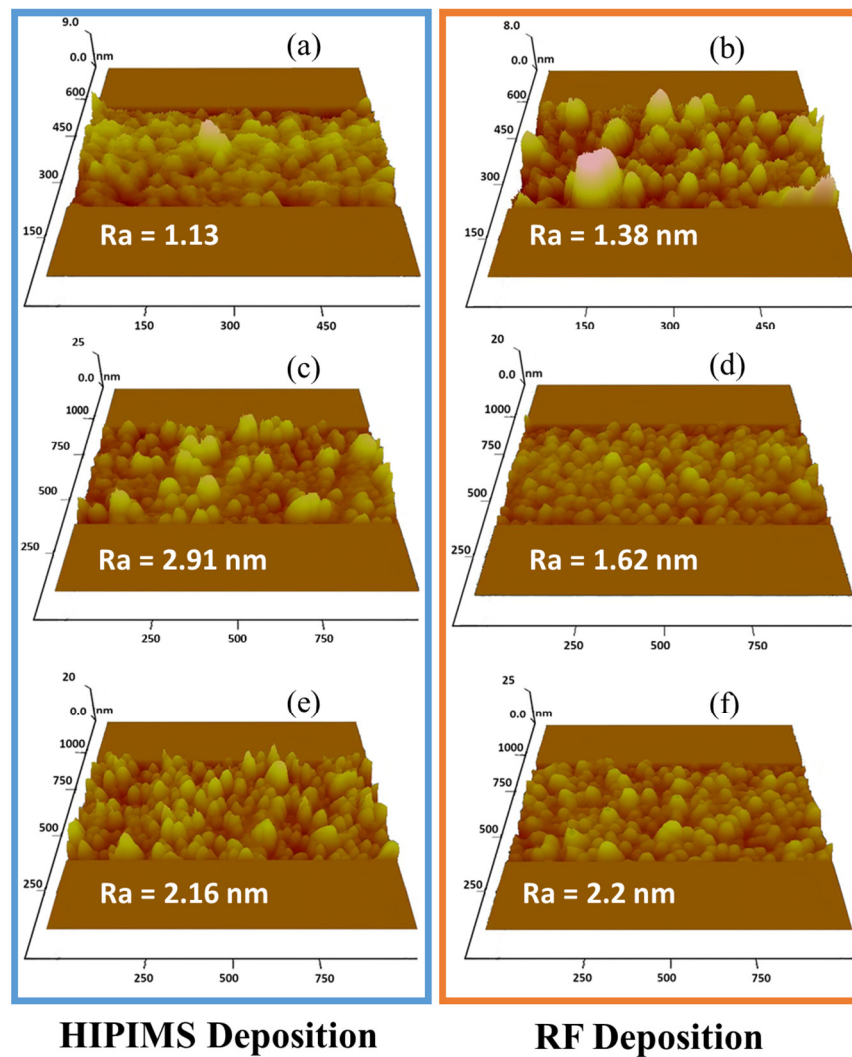
Figure 4. AFM-generated surface morphology plots, including the average roughness value of each deposition. (**a**): 50 W HiPIMS, (**b**) 50 W RF, (**c**) 100 W HiPIMS, (**d**) 100 W RF, (**e**) 150 W HiPIMS, (**f**) 150 W RF.

3.4. Optical Measurement

The optical parameters of the thin films were then examined. Using a spectrometer, the baseline absorption of the glass substrate was first taken, then optical transmission of the films was measured from 300 nm to 800 nm. Using the transmission data, a Tauc plot was created to determine the band gap of each of the films [20]. The absorption coefficient α was first plotted using the equation:

$$\alpha = \frac{-2.303}{t} \log_{10}(\%T) \tag{4}$$

where T is the transmission and t is the GZO film thickness. The following equation was then used to estimate the optical band gap (E_g):

$$(\alpha h v)^{\frac{1}{n}} = B\left(h v - E_g\right) \tag{5}$$

where B is an arbitrary constant and hv is the photon energy, and n will have a value of $\frac{1}{2}$ or 2 depending on if it is a direct or indirect semiconductor, respectively [21]. Utilizing both Equations (2) and (3), the band gap was calculated as shown in Figure 5. The band gap is

obtained by extrapolating the linear regions of the curve to the corresponding horizontal energy axis.
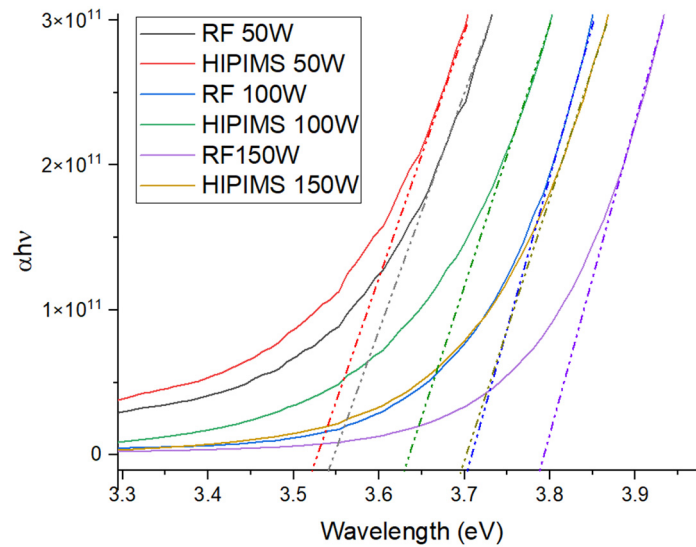
Figure 5. Tauc plot used to determine the band gap of each of the samples.

The increase in band gap with deposition power is likely due to two factors. The first is the Burstein–Moss effect in which increases in the dopant can result in an increase in the band gap. In GZO thin films, an increase in the deposition power increases the concentration of incorporated dopants in the film, yielding a wider band gap [22,23]. The second cause is stress in the film. In GZO thin films, decreasing compressive stress can increase the band gap because compressive stress increases the valance band maximum. As the stress becomes more tensile, the O 2p and Zn 3d, which make up the valance band, become more local, thereby increasing the band gap [24].

It can be seen in Figure 5 that the band gap increases with the increasing average power of the deposition. Consistently, the band gap was greater for the RF depositions reaching a maximum of 3.79 eV for the 150 W RF deposition.

As estimated from the XRD data, increasing the deposition power from 50 W to 150 W for both deposition methods decreased the in-plane compressive film stress, which acted to increase the band gap. In a direct comparison for each deposition power, the HiPIMS films exhibited a higher level of compressive stress which would serve as a band-narrowing mechanism. The comparatively narrower band gap of the HiPIMS deposition may in part be due to an increase in oxidizability of the oxygen in the target material due to the high instantaneous power of the HiPIMS process leading to fewer oxygen vacancies in the film as occurs during HiPIMS deposition of ITO [25]. Doped zinc oxide's available charge carriers are due to both the substitutional atom, such as gallium and interstitial zinc, and oxygen vacancies [26]. The decrease in charge carriers due to a decrease in oxygen vacancies in the HiPIMS deposition would contribute to a narrower band gap as compared to the RF deposition.

The refractive index of the two 150 W depositions was compared using the peaks in the transmission data. This calculation can be performed using the formula [27]:

$$\frac{1}{2\eta t} = \frac{1}{\lambda_{m+1}} - \frac{1}{\lambda_m} \tag{6}$$

where t is the film thickness, η is the refractive index, and λ_{m+1} and λ_m are the wavelengths where the peaks in transmission occur for the samples. The graph of the transmission peaks can be seen in Figure 6.
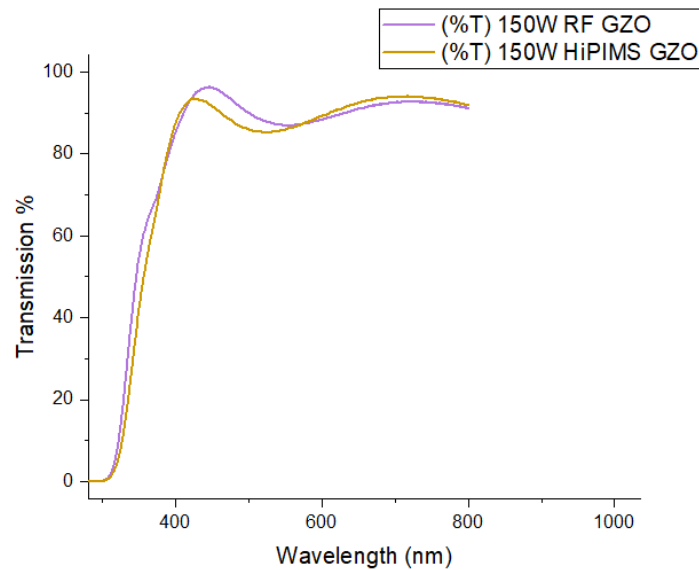
Figure 6. Graph comparison of RF and HiPIMS transmission.

The refractive index of the RF 150 W deposition was found to be 2.45, and the HiPIMS deposition was found to be 2.4. These results are within the range of values to be expected in sputtered GZO [28].

3.5. Electrical

Using the hot probe test, it was found that all films exhibited n-type behavior as expected. The resistivity of the films was measured using a 4-point probe and based on the thickness of the films. The plots of the resistivities of the HiPIMS and RF depositions can be viewed in Figure 7.
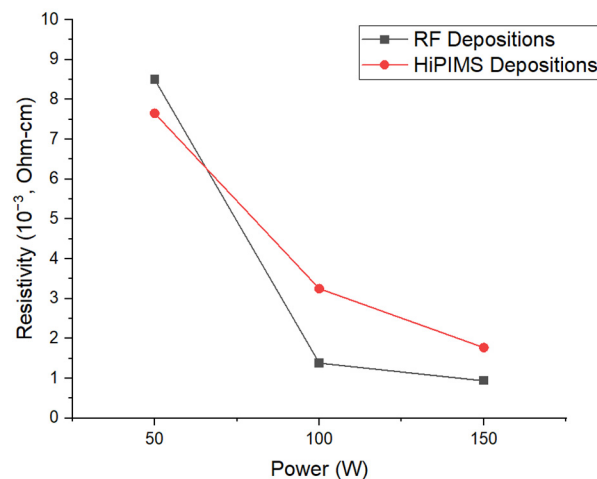
Figure 7. Resistivity vs. average power of deposition.

The decrease in resistivity with increasing average power is likely due to the increased incorporation of Ga+3 ions, whether interstitial or substitutional, in place of the Zn2+ sites, as reported by [29]. The conductivity also can be seen increasing with the surface grain size as measured from the SEM imaging. The higher resistivity value exhibited by the HiPIMS deposition may be due to a reduced number of oxygen vacancies as mentioned in the optical measurement section.

4. Conclusions

In this paper, thin films of GZO deposited by both RF and HiPIMS magnetron sputtering have been compared in structural, optical, and electrical properties. Both the HiPIMS and RF depositions were compared across average deposition power spanning from 50 W to 150 W. It was found that the depositions produced very similar results for equivalent values of average power. It is worth noting that in several parameters, the RF deposition outperformed the HiPIMS process, possessing a higher deposition rate, lower resistivity, wider band gap, and lower average absorption coefficient.

Author Contributions: Conceptualization, J.R.P. and R.A.; Investigation, J.R.P. and A.K.S.; Writing—original draft preparation, J.R.P.; Writing—review & editing, J.R.P., A.K.S., R.A. and K.B.S.; Supervision, R.A. and K.B.S.; Resources, R.A. and K.B.S.; Formal analysis, J.R.P.; Methodology, J.R.P. and A.K.S.; Data curation, J.R.P.; Project administration, R.A. All authors have read and agreed to the published version of the manuscript.

Funding: This research received no external funding.

Institutional Review Board Statement: Not applicable.

Informed Consent Statement: Not applicable.

Data Availability Statement: The experimental data used in this paper will be shared by the corresponding author upon reasonable request.

Conflicts of Interest: The authors declare no conflict of interest.

References

1. Liu, H.; Avrutin, V.; Izyumskaya, N.; Özgür, Ü.; Morkoç, H. Transparent conducting oxides for electrode applications in light emitting and absorbing devices. *Superlattices Microstruct.* **2010**, *48*, 458–484. [CrossRef]
2. Saikumar, A.K.; Skaria, G.; Sundaram, K.B. ZnO gate based MOSFETs for sensor applications. *ECS Trans.* **2014**, *61*, 65. [CrossRef]
3. Saikumar, A.K.; Sundaresh, S.; Sundaram, K.B. Preparation and Characterization of p-Type Copper Gallium Oxide ($CuGaO_2$) Thin Films by Dual Sputtering Using Cu and Ga_2O_3 Targets. *ECS J. Solid State Sci. Technol.* **2022**, *11*, 065010. [CrossRef]
4. Minami, T. Transparent conducting oxide semiconductors for transparent electrodes. *Semicond. Sci. Technol.* **2005**, *20*, S35. [CrossRef]
5. Tanaka, A.; Hirata, M.; Kiyohara, Y.; Nakano, M.; Omae, K.; Shiratani, M.; Koga, K. Review of pulmonary toxicity of indium compounds to animals and humans. *Thin Solid Film.* **2010**, *518*, 2934–2936. [CrossRef]
6. Asvarov, A.; Abduev, A.; Akhmedov, A.; Abdullaev, A. Effects of a high humidity environment and air anneal treatments on the electrical resistivity of transparent conducting ZnO-based thin films. *Phys. Status Solidi C* **2010**, *7*, 1553–1555. [CrossRef]
7. Mahmoudiamirabad, Z.; Eshghi, H. Achievements of high figure of merit and infra-red reflectivity in SnO_2: F thin films using spray pyrolysis technique. *Superlattices Microstruct.* **2021**, *152*, 106855. [CrossRef]
8. Peng, S.; Wang, W.; Yao, T.; Guan, M.; Gan, Z.; Chu, J.; Gai, L. Excellent Properties of Ga-doped ZnO Film as an Alternative Transparent Electrode for Thin-Film Solar Cells. *Int. J. Appl. Glass Sci.* **2022**, *14*, 133–139. [CrossRef]
9. Peng, S.; Yao, T.; Yang, Y.; Zhang, K.; Jiang, J.; Jin, K.; Li, G.; Cao, X.; Xu, G.; Wang, Y. Influences of the RF power ratio on the optical and electrical properties of GZO thin films by DC coupled RF magnetron sputtering at room temperature. *Phys. B Condens. Matter* **2016**, *503*, 111–116. [CrossRef]
10. Ellmer, K. Magnetron sputtering of transparent conductive zinc oxide: Relation between the sputtering parameters and the electronic properties. *J. Phys. D Appl. Phys.* **2000**, *33*, R17. [CrossRef]
11. Lundin, D.; Sarakinos, K. An introduction to thin film processing using high-power impulse magnetron sputtering. *J. Mater. Res.* **2012**, *27*, 780–792. [CrossRef]
12. Ghailane, A.; Makha, M.; Larhlimi, H.; Alami, J. Design of hard coatings deposited by HiPIMS and dcMS. *Mater. Lett.* **2020**, *280*, 128540. [CrossRef]
13. Mickan, M.; Helmersson, U.; Rinnert, H.; Ghanbaja, J.; Muller, D.; Horwat, D. Room temperature deposition of homogeneous, highly transparent and conductive Al-doped ZnO films by reactive high power impulse magnetron sputtering. *Sol. Energy Mater. Sol. Cells* **2016**, *157*, 742–749. [CrossRef]
14. Wu, B.; Haehnlein, I.; Shchelkanov, I.; McLain, J.; Patel, D.; Uhlig, J.; Jurczyk, B.; Leng, Y.; Ruzic, D.N. Cu films prepared by bipolar pulsed high power impulse magnetron sputtering. *Vacuum* **2018**, *150*, 216–221. [CrossRef]
15. Starfire Industries, LLC. *IMPULSE™ 2-2 Pulsed Power Module Operation Manual*; Starfire Industries, LLC: Champaign, IL, USA, 2019.
16. Mareš, P.; Dubau, M.; Polášek, J.; Mates, T.; Kozák, T.; Vyskočil, J. High deposition rate films prepared by reactive HiPIMS. *Vacuum* **2021**, *191*, 110329. [CrossRef]

17. Khranovskyy, V.; Grossner, U.; Nilsen, O.; Lazorenko, V.; Lashkarev, G.V.; Svensson, B.G.; Yakimova, R. Structural and morphological properties of ZnO: Ga thin films. *Thin Solid Film.* **2006**, *515*, 472–476. [CrossRef]

18. Bindu, P.; Thomas, S. Estimation of lattice strain in ZnO nanoparticles: X-ray peak profile analysis. *J. Theor. Appl. Phys.* **2014**, *8*, 123–134. [CrossRef]

19. Lim, W.T.; Lee, C.H. Highly oriented ZnO thin films deposited on Ru/Si substrates. *Thin Solid Film.* **1999**, *353*, 12–15.

20. Tauc, J.; Grigorovici, R.; Vancu, A. Optical properties and electronic structure of amorphous germanium. *Phys. Status Solidi* **1966**, *15*, 627–637. [CrossRef]

21. Roy, S.; Ghosh, M.P.; Mukherjee, S. Introducing magnetic properties in Fe-doped ZnO nanoparticles. *Appl. Phys. A* **2021**, *127*, 451. [CrossRef]

22. Zhu, Y.; Wu, Y.; Cao, F.; Ji, X. Ga-concentration-dependent optical and electrical properties of Ga-doped ZnO thin films prepared by low-temperature atomic layer deposition. *J. Mater. Sci. Mater. Electron.* **2022**, *33*, 5696–5706. [CrossRef]

23. Akin, N.; Kinaci, B.; Ozen, Y.; Ozcelik, S. Influence of RF power on the opto-electrical and structural properties of gallium-doped zinc oxide thin films. *J. Mater. Sci. Mater. Electron.* **2017**, *28*, 7376–7384. [CrossRef]

24. Wang, Y.; Tang, W.; Liu, J.; Zhang, L. Stress-induced anomalous shift of optical band gap in Ga-doped ZnO thin films: Experimental and first-principles study. *Appl. Phys. Lett.* **2015**, *106*, 162101. [CrossRef]

25. Zhao, M.-J.; Zhang, J.-F.; Huang, J.; Huang, Q.-H.; Wu, W.-Y.; Tseng, M.-C.; Huang, C.-J.; Kuo, H.-C.; Lien, S.-Y.; Zhu, W.-Z. Effect of power density on compositional and structural evolution of ITO thin film by HiPIMS method. *Vacuum* **2022**, *200*, 111034. [CrossRef]

26. Zhang, P.; Hong, R.; Chen, Q.; Feng, W. On the electrical conductivity and photocatalytic activity of aluminum-doped zinc oxide. *Powder Technol.* **2014**, *253*, 360–367. [CrossRef]

27. Carreño, F.; Martínez-Antón, J.C.; Bernabeu, E. Optical interference method to obtain thickness and refractive indices of a uniaxial medium. *Rev. Sci. Instrum.* **1994**, *65*, 2489–2493. [CrossRef]

28. Mahdhi, H.; Gauffier, J.L.; Djessas, K.; Ayadi, Z.B. Thickness dependence of properties Ga-doped ZnO thin films deposited by magnetron sputtering. *J. Mater. Sci. Mater. Electron.* **2017**, *28*, 5021–5028. [CrossRef]

29. Mahdhi, H.; Ben Ayadi, Z.; Gauffier, J.L.; Djessas, K.; Alaya, S. Influence of sputtering power on the properties of thin layers of GZO for photovoltaic applications. *J. Mater. Sci. Mater. Electron.* **2015**, *26*, 3336–3343. [CrossRef]